HIGH-TEMPERATURE FRICTION WEAR BEHAVIOR OF (AlB$_2$ + Al$_2$O$_3$)/A356 COMPOSITES REGULATED BY ACOUSTIC-MAGNETIC COUPLING FIELD

Lei Jiao [ORCID], **Qinjun Zhang, Yutao Zhao, Fan Li, Baowang Wang, Zhiwen Wang and Chengyong Xu**
School of Materials Science and Engineering, Jiangsu University, Zhenjiang 212013, People's Republic of China

Hui Li
School of Materials Science and Engineering, Jiangsu University of Science and Technology, Zhenjiang 212003, People's Republic of China

Sheretskyi Volodymyr
Institute of Physics and Technology of Metals and Alloys, National Academy of Sciences of Ukraine, Kyiv, Ukraine

Abstract

In this paper, the A356-B$_2$O$_3$-KBF$_4$ system was designed, and (AlB$_2$ + Al$_2$O$_3$)/A356 in situ dual-phase reinforced particle composites with mass fractions of 2 wt%, 4 wt%, 6 wt% and 8 wt% were prepared by the DMR method. The acoustic-magnetic coupling control was carried out during the preparation of 6 wt% (AlB$_2$ + Al$_2$O$_3$)/A356 composite. XRD, PC, SEM, EDS, and dry friction tests studied the composites' microstructure and high-temperature wear properties. The results show that the matrix α-Al grains of the composite are refined under the action of the coupling field, with a grain size of: 94.3 um. The AlB$_2$ particles are rod-shaped with a radial size of 11 um, and the Al$_2$O$_3$ particles are nano-sized flakes. The wear mechanism of (AlB$_2$ + Al$_2$O$_3$)/A356 dual-phase in situ aluminum matrix composites is high-temperature oxidation abrasive wear, which differs from the adhesive wear of the matrix alloy.

Due to the anti-friction, lubrication and anti-wear effects of the dual-phase in situ particles (AlB$_2$ + Al$_2$O$_3$), the wear resistance of the composites is improved, and the coefficient of friction is reduced by 13.4% compared to the A356 matrix alloy. With the increase in temperature, the wear resistance of 6 wt% (AlB$_2$ + Al$_2$O$_3$)/A356-1 kW-10 Hz composite was substantially better than that of the A356 matrix alloy. The wear rate of the composite at different temperatures was reduced by 8.82% (100 °C), 11.29% (200 °C), and 13.69% (300 °C), respectively, compared with that of the matrix A356.

Keywords: A356-B$_2$O$_3$-KBF$_4$ system, acoustic-magnetic coupling, composite material, duplex particles, friction and wear behavior

Introduction

Aluminum alloys are widely used in the aerospace and automotive industries due to their superior properties, such as high specific strength, excellent low-temperature performance, excellent corrosion resistance, chemical inertness and other excellent properties.[1] However, the disadvantages of high-temperature resistance and poor wear performance of aluminum alloy limit its application. In order to improve the performance of conventional aluminum alloys, aluminum alloys reinforced by ceramic particles have been developed, called particle-reinforced aluminum matrix composites.[2–5]

Particulate-reinforced aluminum matrix composites (PAMCs) are widely used and have significant advantages over fiber-reinforced aluminum matrix composites, such as isotropic, simple and mature preparation processes and low cost.[6,7] In addition, PAMC can be secondary molded using conventional processing methods.[8–10]

PAMCs have a higher specific strength, specific stiffness and wear resistance than aluminum alloy matrix.[11–16] Most of the traditional research has focused on the addition of

single anti-wear particles or lubricated wear-reducing particles to enhance the wear resistance of the material.[17–22] Bai et al.[23] studied the effect of Al_2O_3 particles on the friction and wear behavior of 7075 aluminum alloy. The results show that the friction and wear properties of the composites reach the highest when the mass fraction of Al_2O_3 particles reaches 5%. The wear mechanism at room temperature is slightly abrasive wear. The addition of Al_2O_3 can improve the wear resistance of the material. Yang et al.[24] studied the effect of particle size on friction and wear behavior. Studies have shown that when Al_2O_3 particles are nano-sized, the wear rate and friction coefficient of the material decrease, and the increase in particle size will increase the degree of abrasive wear and reduce the material's wear resistance. Agrawal et al.[25] found that the dispersed TiB_2 particles have a refining effect on α-Al grains and have a significant effect on the hardness, tensile strength and dry sliding wear resistance of the material by adding magnetic field stirring during melt solidification. Yuan et al.[26] fabricated AlB_2 particle-reinforced aluminum matrix composites. Experiments show that the in situ generated AlB_2 particles significantly improve the wear resistance of pure aluminum and that adding AlB_2 has a significant friction-reducing effect. However, there are few reports on introducing dual-phase particles 'anti-wear[27] and anti-friction[27,28]' mechanisms to improve the wear performance of materials. Therefore, this paper designs to introduce AlB_2 and Al_2O_3 dual-phase in situ particles to improve the performance of A356 aluminum alloy materials by the direct melt reaction (DMR) method.

In situ PAMCs have the advantages of a clean interface and low process costs compared to applied particle PAMCs. As the research progresses, the preparation cost of aluminum in situ PAMCs is still decreasing, and in situ PAMCs can meet the requirements of lightweight, good designability, and low preparation cost, which makes aluminum in situ PAMCs can be used in military and civil fields, especially in vehicles, aerospace, and electronic packaging industries which have broad application prospects.

However, in situ particles as reinforcing phases in the aluminum matrix can have uneven distribution, coarse particles, and other undesirable conditions. Therefore, exploring new methods to overcome the problems related to particle formation in aluminum matrix composites has become an essential direction for materials research.[29] The effect of external fields on particle morphology and distribution is investigated by adding an external field to an in situ particle reaction. Standard methods include mechanical stirring, electromagnetic stirring and high-energy ultrasonic fields.[30–34] The role of a single external physical field is limited, each has its advantages and disadvantages, and multi-field coupling has become a new trend.[35,36]

Acoustic-magnetic coupling of external physical fields is the more popular combination of multi-field coupling.[37] In recent years, many scientists have successfully fabricated in situ particle-reinforced aluminum matrix composites using the acoustic-magnetic coupling-assisted mixed salt reaction method. Tao et al.[38,39] investigated the effect of the acoustic-magnetic coupling field on the dispersion of ZrB_2 particles by adding an acoustic-magnetic coupling field during the in situ reaction and found that the acoustic-magnetic coupling field had a significant effect on the nanoparticle distribution and particle number increase. The nanoparticles are refined, and the distribution is improved. The coupling of ultrasound and magnetic field not only solves the problems of a single physical field, but also enlarges the advantages of a single physical field. Zhang et al.[40] produced Al_2O_3 and Al_3Zr by in situ reaction with the assistance of a pulsed magnetic field, with more uniform particle distribution, smaller particle size, and the number of in situ particles increased, which is much more nuanced than that without the assistance of pulsed magnetic field. Kai et al.[41] prepared ZrB_2/Al nanocomposites with ultrasonic vibration and helical electromagnetic stirring. Ultrasonic vibrations prevent the rapid growth of in situ synthesized nanoparticles in the melt and disrupt clustering, resulting in smaller sizes (10–50 nm) and relatively more uniform distribution of in situ nanoparticles in the final composite grains at the boundaries and/or inside the aluminum matrix.

In this paper, $(AlB_2 + Al_2O_3)$/A356 composites with mass fractions of 2 wt%, 4 wt%, 6 wt% and 8 wt% were designed and prepared by the DMR method using A356-B_2O_3-KBF_4 system. The acoustic-magnetic coupling control was carried out during the preparation of 6 wt% $(AlB_2 + Al_2O_3)$/A356 composite. XRD, PC, SEM and, EDS analyzed the morphology, distribution and, size of AlB_2 and Al_2O_3 particles. The high-temperature frictional wear behavior and mechanism of the 6 wt% $(AlB_2 + Al_2O_3)$/A356-T6-1 kW-10 Hz dual-phase composite was investigated by dry sliding frictional wear experiments.

Table 1. A356 Alloy Ingot Chemical Composition (wt%)

Elements	Si	Mg	Ti	Fe	Mn	Cu	Zn	Sn	Pb	Al
Components	7.39	0.37	0.16	0.1	0.05	0.05	0.05	0.01	0.03	91.79

Experimental Procedure

Sample Preparation

The raw materials are A356 alloy ingots and inorganic salts KBF_4 and B_2O_3 powders. The experimental method is the in situ reaction. The composition of the A356 alloy is shown in Table 1. The reaction equation is as follows:

$$2KBF_4 + 4Al + B_2O_3 = 2AlB_2 + Al_2O_3 + 2KAlF_4$$
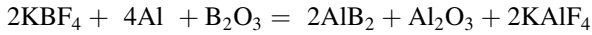
Calculate the mass of B_2O_3 powder and KBF_4 powder required to determine x wt% $(AlB_2 + Al_2O_3)$/A356 (x = 2, 4, 6, 8). The two inorganic salt powders were dried at 250 °C for 2.5 h and mixed in a mortar. The A356 alloy ingot was melted and superheated to 850 °C by a high-frequency induction furnace, and the mixed salts were pressed into the molten aluminum with graphite bellows and held for 30 min. After the reaction, the C_4Cl_4 refining agent was added to the melt for drossing and degassing. Wait for the melt to cool down to 720 °C and cast the melt into the preheated iron mold to obtain the composite. After microstructure observation, the optimum particle mass fraction for composite preparation was determined by comparing the matrix grain size and the amount and distribution of particles produced for each mass fraction. When the particle mass fraction reaches the best, the grain size of the matrix is the smallest, and the distribution of the particles is more uniform. The agglomeration of the particles at the grain boundary is the slightest, and the particles play the best role in refining the matrix grains and strengthening the matrix.

Based on the optimum mass fraction, four portions of B_2O_3 powder and KBF_4 powder were taken and dried at 250 °C for 2.5 h, and the two inorganic salts were ground and mixed in a mortar. The A356 alloy ingot was melted and superheated to 850 °C by a high-frequency induction furnace. The mixed salt is pressed into the molten aluminum solution with a graphite bell for the reaction, with magnetic field strengths of 5 Hz, 10 Hz and 15 Hz and an ultrasonic field power of 1 kW. The reactions were held for 30 min under different applied physical fields (no external field, 1 kW–5 Hz, 1 kW–10 Hz, and 1 kW–15 Hz). The acoustic-magnetic coupling field was applied every 5 min for a total of six times, each time for 30 s. Figure 1 shows schematic diagrams of laboratory equipment. After the reaction, the C_4Cl_4 refining agent was added to the melt for drossing and degassing. Wait for the melt to cool to 720 °C, and cast the melt into the iron mold preheated at 200 °C for 20 min to get the composite material.

Physical Phase Analysis

The material was analyzed by D8 ADVANCE X-ray diffractometer (XRD), and the XRD specimens were cut into 10 mm * 10 mm * 3 mm specimens by wire cutting. Sandpaper was used to smooth the specimens to the same height as the specimen table.

The test diffraction angle parameter is 20°–90°, and the test speed is 2°/min.

Polarization Analysis

The Leica DM750P polarized light microscope was used to analyze the material organization, and the Image Pro Plus software was used to quantify the grain size of the material. The specimens were cut into cubes of 10 mm * 10 mm * 10 mm using wire cutting, and the surfaces of the specimens were sanded using 400#, 600#, 800#, 1000#, 1200#, 1500#, and 2000# sandpaper. Polishing was carried out on the P-1 metallographic specimen polishing machine until there was no scratches on the surface of the specimen. Subsequently, under the condition of 22 V voltage and 0.1–0.2 mA current, the anode film was carried out on the surface of the sample using the coating solution (the ratio
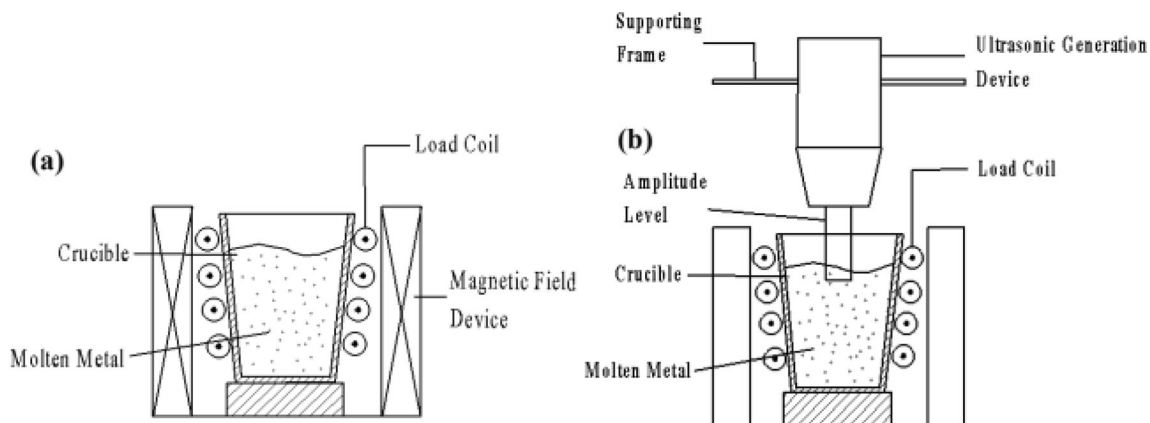
Figure 1. Schematic diagrams of laboratory equipments: (a) electromagnetic stirring device; (b) ultrasonic vibration device.

of the coating solution is: $H_2SO_4:H_3PO_4:H_2O = 43:38:19$) for 1.5–2 min.

SEM Analysis

In this experiment, the microstructure of the prepared composites was observed and analyzed by FEI Nova-Nano450 field emission scanning electron microscope. The dispersion of in situ endogenous particles and the particle size was observed, and the morphology of the friction wear specimens was analyzed.

The 3D Confocal Analysis Performed

The abrasion of friction wear samples was analyzed by LEXT OLS400 3D confocal microscope. A 3D confocal microscope measured the average cross-sectional area of the ground mark, and the formula calculated the wear rate of the sample.

$$K = \frac{C \times S}{F \times L}$$

where C is the wear circumference; S is the cross-sectional area of the wear; F is the load; and L is the length of the wear mark.

T6 Heat Treatment

The materials used for the high-temperature friction wear behavior investigation were solution treated at 540 °C for 5 h. The specimens after solid solution treatment were rapidly cooled in water at 60 °C and placed in an oven at 170 °C for 24 h of aging treatment. In the 24-h aging treatment process, the specimens were subjected to Vickers hardness tests hourly to derive the peak aging parameters.

Room Temperature Friction and Wear

In this experiment, the friction and wear test samples were prepared by wire cutting, and the surface of the samples was polished with 400#, 600#, 800#, 1000#, 1200#, 1500#, and 2000# sandpaper. The test piece was polished with a diamond metallographic polishing agent with a particle size of 0.5 um on a P-1 metallographic sample polishing machine. Finally, after polishing, the friction and wear test samples were subjected to room temperature friction and wear experiments on the HT-1000 high-temperature friction and wear tester. The opposite surface of the friction is the steel plate, and the wear diameter is 4 mm. The friction loads were 5 N, 10 N, and 15 N, and the friction speeds were 200 rpm, 250 rpm, and 300 rpm. Table 2 shows the specific friction and wear experimental parameters.

Table 2. Room Temperature Friction and Wear Test Parameters

Revolution speed (rpm)	Load (N)	Time (min)	Friction radius (mm)
200	5	20	4
200	10	20	4
200	15	20	4
250	10	20	4
300	10	20	4

High-Temperature Friction Wear

The T6-treated composites with A356 alloy and A356-T6 were cut into friction wear test specimens using a wire cutter, and the surfaces were sanded using 400#, 600#, 800#, 1000#, 1200#, 1500# and 2000# sandpaper. The polished test piece was polished on the P-1 metallographic sample polishing machine with diamond metallographic polish with a grain size of 0.5 um. Finally, the polished friction and wear test specimens are subjected to high-temperature friction and wear test on HT-1000 high-temperature friction and wear tester. The opposite surface of the friction is the steel plate, and the wear diameter is 4 mm. The friction load and rotational speed were 10 N and 200 rpm, respectively. The friction temperatures were 100 °C, 200 °C and 300 °C, respectively. Each material was tested three times, and the average value was taken to obtain the final results.

Characterization

XRD Analysis

The study analyzed $(AlB_2 + Al_2O_3)$/A356 composites with mass fractions ranging from 2 to 8 wt% and A356 aluminum alloy using XRD. XRD measurements were performed using a copper target. The diffraction angle parameter is 20°–90°, the test speed is 2°/min, the step size is 0.02°, and the dwell time is 2 s. MDI Jade software, combined with PDF cards, was used for specific experimental data analysis, and origin was used to produce XRD spectra and calibrate the relevant diffraction peaks. Figure 2 displays the XRD results indicating that significant Al and Si peaks are present in all five materials. In addition, the XRD results for the four composites showed several faint peaks, which were analyzed and identified as the Al_2O_3 and AlB_2 phases. The study successfully prepared composites of $(AlB_2 + Al_2O_3)$/A356 with reinforced target AlB_2 particles and Al_2O_3 particles using the melt direct reaction method of the $A356-B_2O_3-KBF_4$ system.

Polarization Analysis

Since the grains of different colors in the polarized micrographs are grains of different orientations, the large and small black areas may be the composites' reinforced particle clusters. Figure 3a–d shows the polarized images of $(AlB_2 + Al_2O_3)/A356$ composites with reinforced
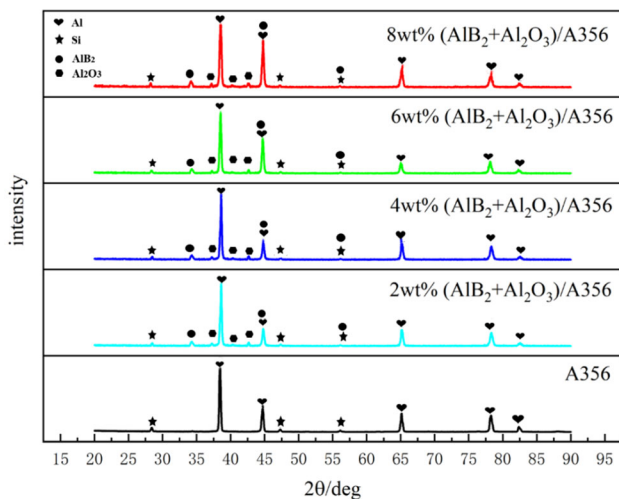

**Figure 2. XRD patterns of A356 alloy and $(AlB_2 + Al_2O_3)/$ A356 composites with different particle contents.**

particle mass fractions of 2 wt%, 4 wt%, 6 wt. % and 8 wt%, respectively. The multiple of the polarized photograph is 100x. ImagePro Plus software calculated the grain size of the randomly sampled polarized photos. Figure 4 displays the results for grain size, which are as follows: 210.34 um, 182.63 um, 160.36 um, and 165.63 um.

The grain size of the A356 matrix alloy decreases with increasing particle mass fraction, with the best refinement effect at a particle mass fraction of 6 wt%. In addition, the particles are mainly distributed along the grain boundaries, and agglomeration is most severe when the particle mass fraction is 8 wt%. This happens because the aluminum crystals in the matrix push the particles toward the grain boundaries during crystallization. As more particles are pushed to the grain boundaries, the particles agglomerate to reduce the surface energy to reduce the overall energy of the system and achieve a stable state. Therefore, when the system synthesizes the composite material, it is necessary to strengthen the stirring or use the external physical field to make the particle distribution uniform and reduce the agglomeration.

In order to verify the effect of the coupling field on the particle distribution and the amount of particle production within the composite, polarization analysis was carried out
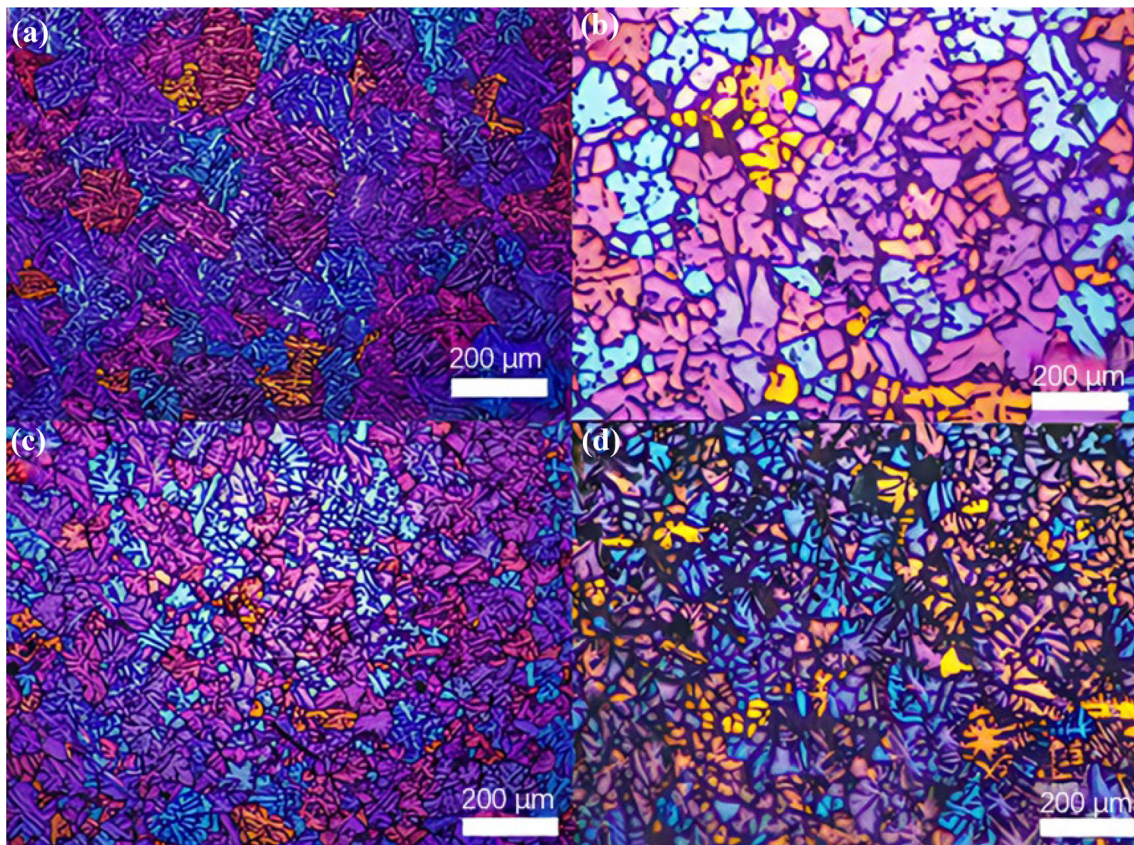
Figure 3. Polarized light micrographs of $(AlB_2 + Al_2O_3)/A356$ composites with different particle contents (a) 2 wt%; (b) 4 wt%; (c) 6 wt%; (d) 8 wt%.
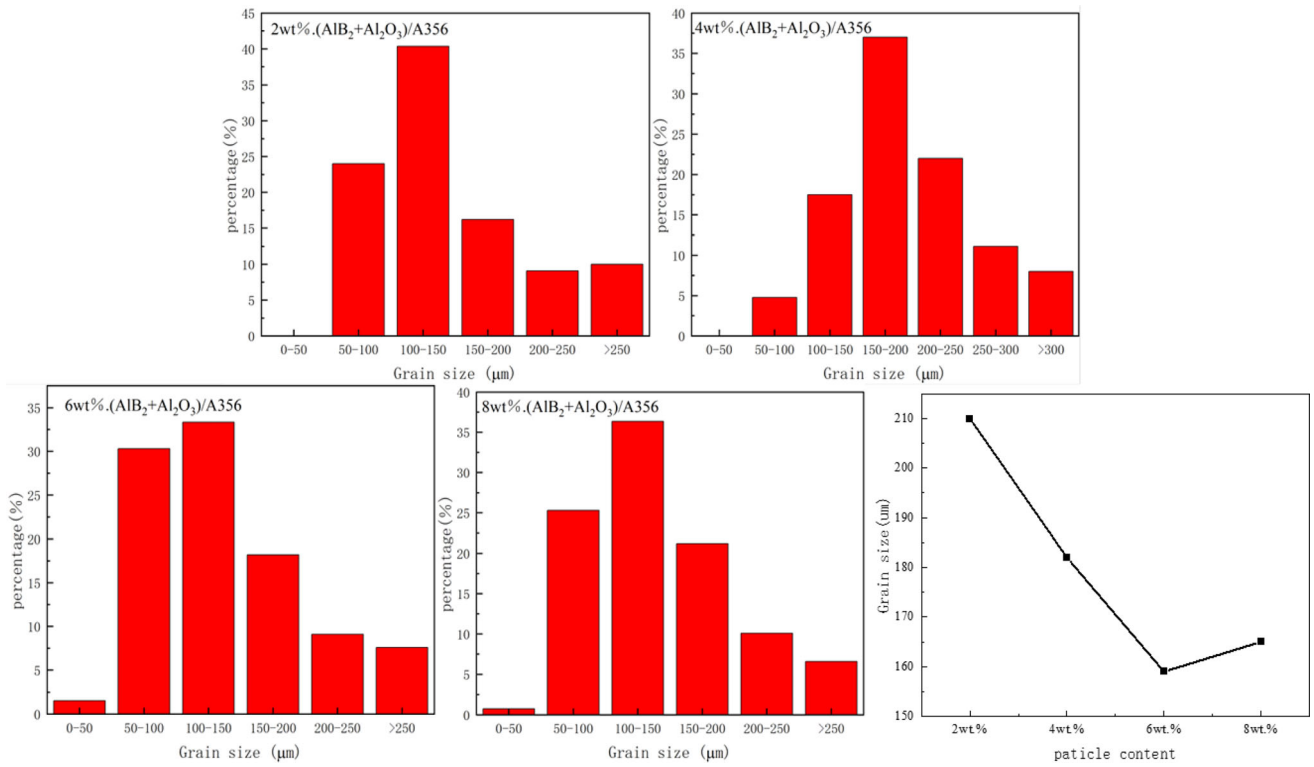
Figure 4. Grain size distribution of different composites.
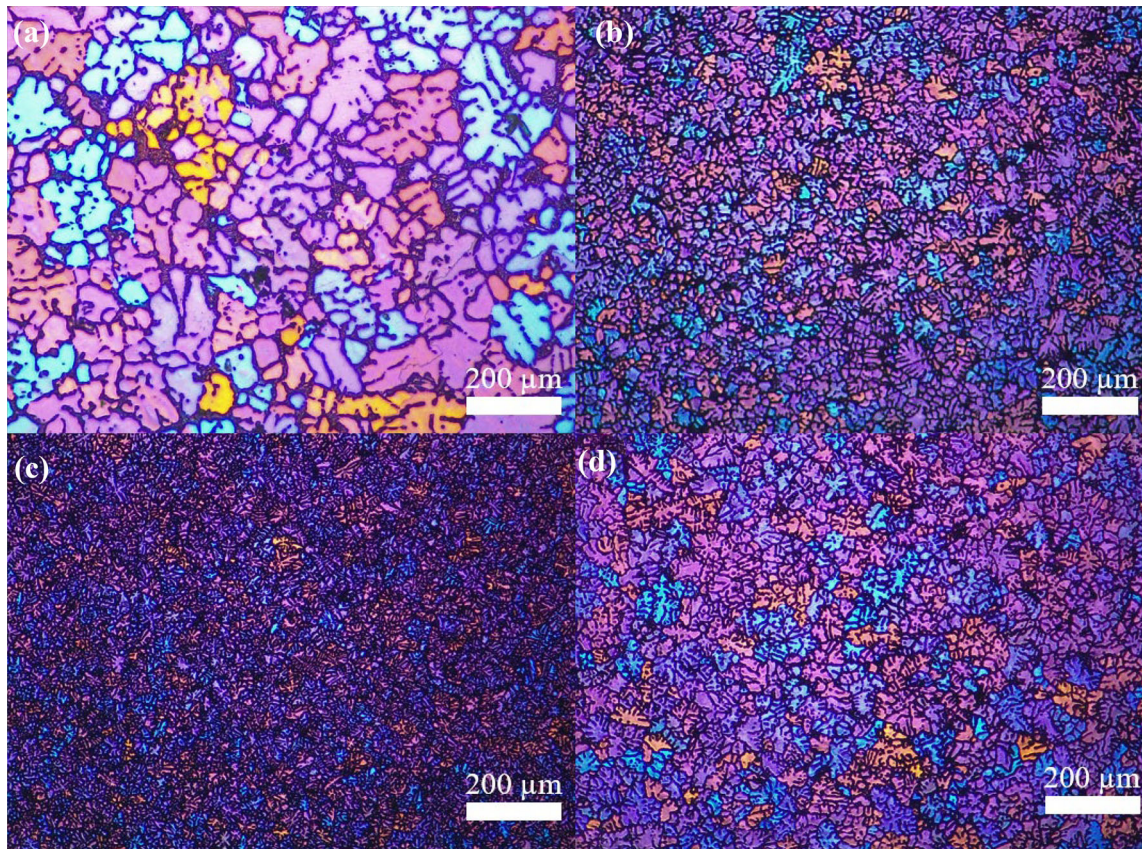
Figure 5. Polarized light images of 6wt% (AlB$_2$ + Al$_2$O$_3$)/A356 composites prepared under different magnetic field frequencies (a) no outfield; (b) 1 kW–5 Hz; (c) 1 kW–10Hz; (d) 1 kW–15 Hz.
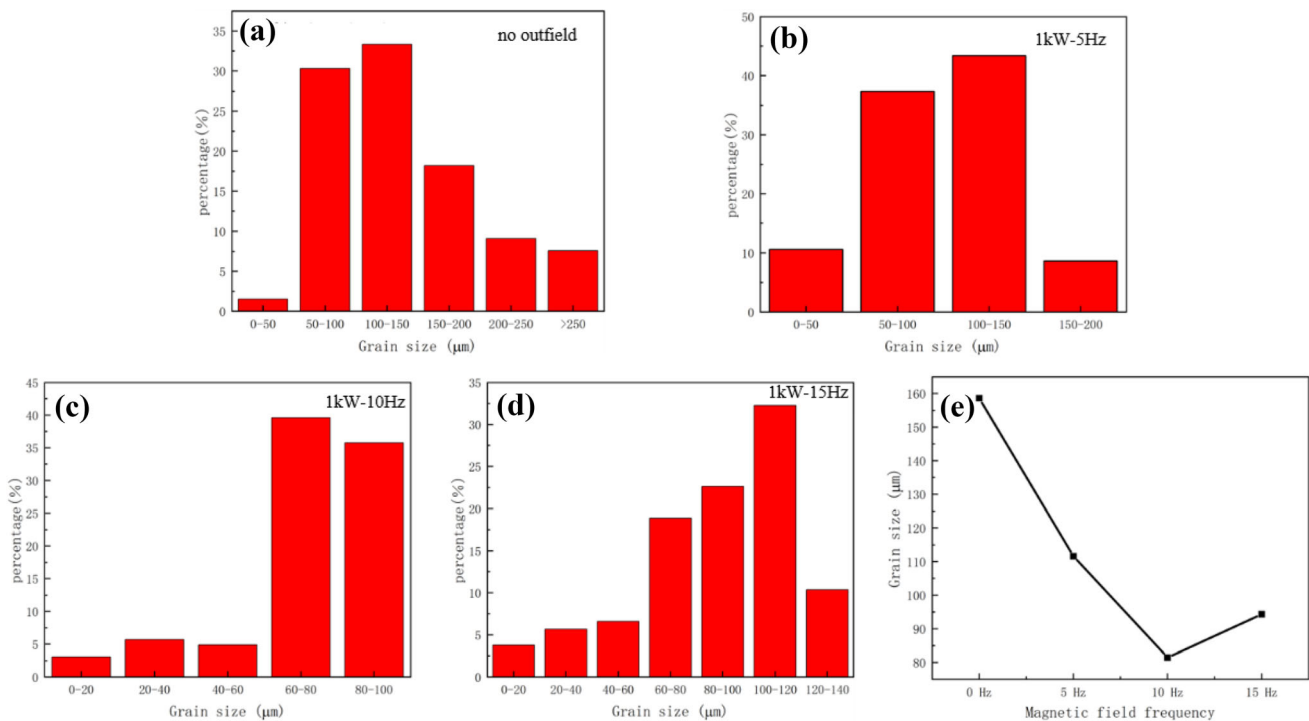
on the 6 wt% (AlB$_2$ + Al$_2$O$_3$)/A356 composite. Figure 5 shows polarized images of the 6 wt% (AlB$_2$ + Al$_2$O$_3$)/A356 composite prepared under different applied magnetic fields at a magnification of 100x. These images provide information on the microstructure of the composites, which is affected by the direction and strength of the magnetic field applied during fabrication. The grain size distribution of the composites is shown in Figure 6, allowing further analysis of the composite structure and properties. The grain sizes of the 6 wt% (AlB$_2$ + Al$_2$O$_3$)/A356 composites were measured using the Imagepro plus software. The calculated sizes were 158.6 um, 111.6 um, 81.5 um, and 94.3 um for the applied physical field data of no outfield, 1 kW–5 Hz, 1 kW–10 Hz, and 1 kW–15 Hz, respectively.

According to Figures 5 and 6, adding an acoustic-magnetic coupling external field control reaction during the preparation process leads to a significant decrease in the grain size of the composite material. The grain size is the smallest when the external physical field data is 1 kW–10 Hz. With the magnetic field frequency increasing, the grain size decreases from 158.6 um at no outfield to 81.5 um at 10 Hz. When the magnetic field frequency is 15 Hz, the grain size increases slightly due to the skin effect of the magnetic field. The grains tend to change from dendritic to equiaxed crystals. This is due to adding in situ dual-phase particles as the core of heterogeneous nuclei. With the increase in magnetic field frequency, the size of in situ dual-phase particles decreases, and the core of heterogeneous nuclei increases. Mutual obstruction during the growth process will inhibit the growth rate so that the tiny grains change from coarse dendrite to equiaxed crystals.

SEM and Energy Spectrum Analysis

Figure 7 shows the SEM image of 6 wt% (AlB$_2$ + Al$_2$O$_3$)/A356 composites prepared at different magnetic field frequencies. The diagram shows many silver-gray or black square or long rod-like small particles. The EDS energy spectrum test results (Figure 7d) show that these long rod-like or block-like objects are AlB$_2$ particles with a radial size of about 11 um. Additionally, a significant number of bright white punctate particles can be observed in the material. The EDS results (Figure 7a) show that these bright white particles are Al$_2$O$_3$ particles, and the radial size is nanoscale. Since the Al$_2$O$_3$ particles are already at the nanoscale, the acoustic-magnetic coupling external field control reaction mainly plays a role in the larger AlB$_2$ particles. Under the same external field conditions, the rotation and collision between AlB$_2$ particles with large size and rod-like morphology are more intense. On the other hand, when Al$_2$O$_3$ particles with a smaller size and rounder shape vibrate in the melt, the relative motion between particles is not as intense as that of AlB$_2$ particles. Figure 7b shows that AlB$_2$ is mainly distributed in the Al matrix in the form of large particles and rods. With the increase in magnetic field frequency, the particle size of AlB$_2$ decreases, and some AlB$_2$ particle clusters in the form of clusters appear. However, when the applied magnetic field reaches 15 Hz, due to the skin effect, the

Figure 6. Grain size distribution of different composites (a) no outfield; (b) 1 kW–5 Hz; (c) 1 kW–10 Hz; (d) 1 kW–15 Hz; (e) average size.
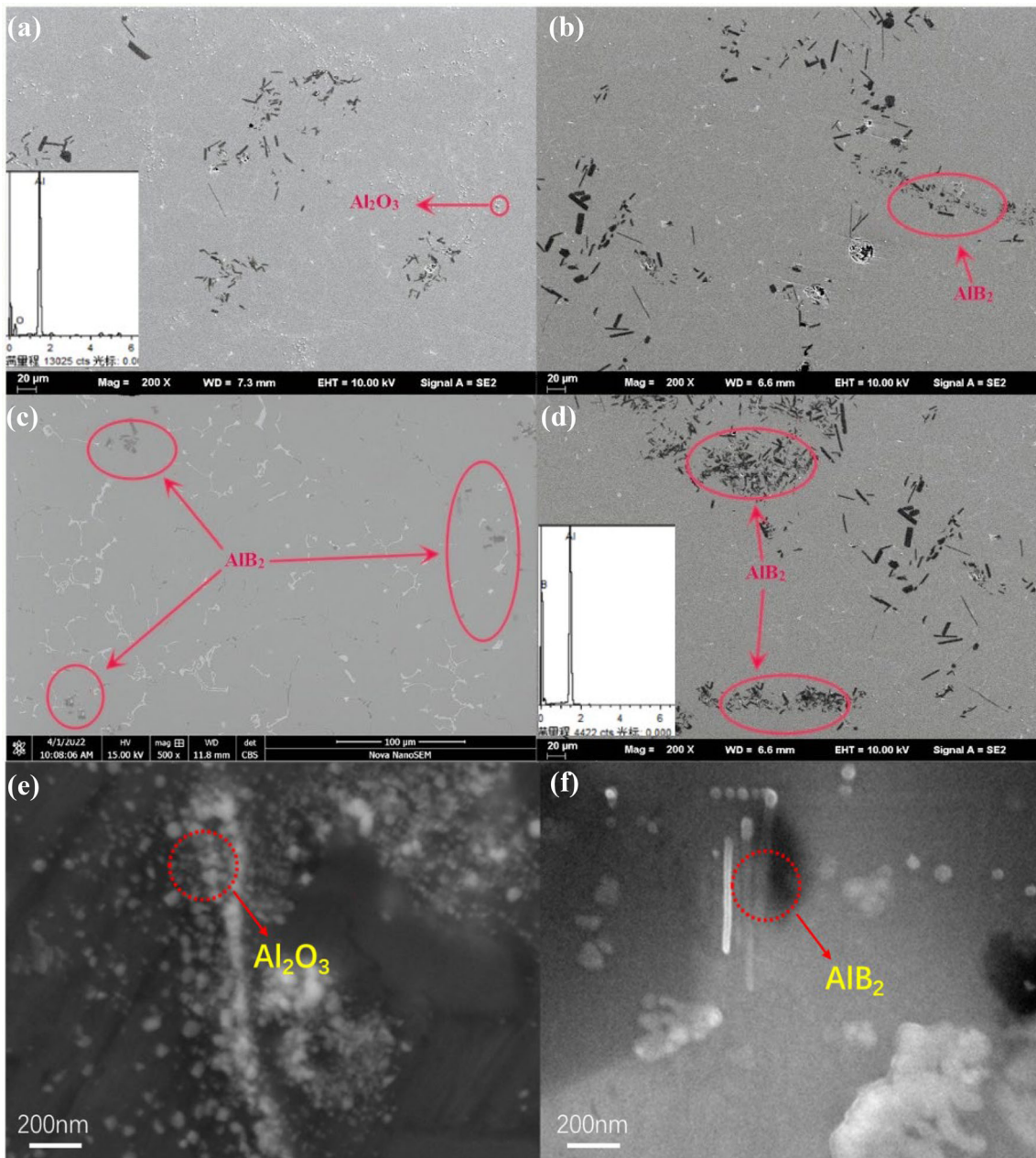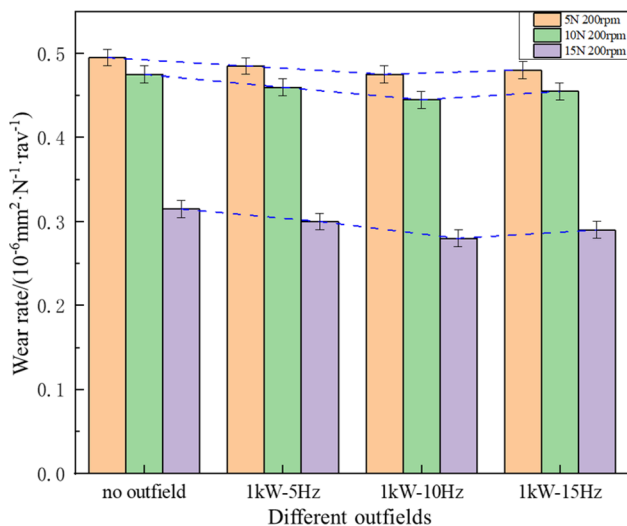
Figure 7. *SEM of 6 wt% (AlB$_2$ + Al$_2$O$_3$)/A356 composites (a, e, f) no outfield; (b) 1 kW–5 Hz; (c)1 kW–10 Hz; (d) 1 kW–15 Hz.*

alternating current generated by the alternating magnetic field in the melt exhibits an uneven distribution with less internal and dense external. If the magnetic field frequency is too high, the magnetization will increase. In situ, endogenous particles migrate outward under strong centrifugation. Long-term magnetic stirring may deteriorate the in situ particle distribution, and the clusters will become too large, affecting the material's performance. In addition, it can be seen from the diagram that the number of particles per unit area also has an increasing trend with the increase in the magnetic field due to the acoustic-

magnetic coupling external field regulation making the reaction more complete.

Figure 7e, f shows 30K-fold SEM images of 6 wt% (AlB$_2$ + Al$_2$O$_3$)/A356 composites to analyze the particle morphology of AlB$_2$ and Al$_2$O$_3$ particles. At 30 K magnification, several circular Al$_2$O$_3$ particles can be found in the nanoscale range. In addition, the red circle marker shown in Figure 7f shows that that the interface between the two particles and the matrix is pure and tightly bonded. Introducing AlB$_2$ and Al$_2$O$_3$ particles refines the matrix grains and plays a role in fine grain strengthening.

Figure 8. Wear rate of 6 wt% (AlB$_2$ + Al$_2$O$_3$)/A356 composites prepared at different magnetic field frequencies composite under different loads.

Figure 9. Wear volume of 6 wt% (AlB$_2$ + Al$_2$O$_3$)/A356 composites prepared at different magnetic field frequencies composite under different loads.
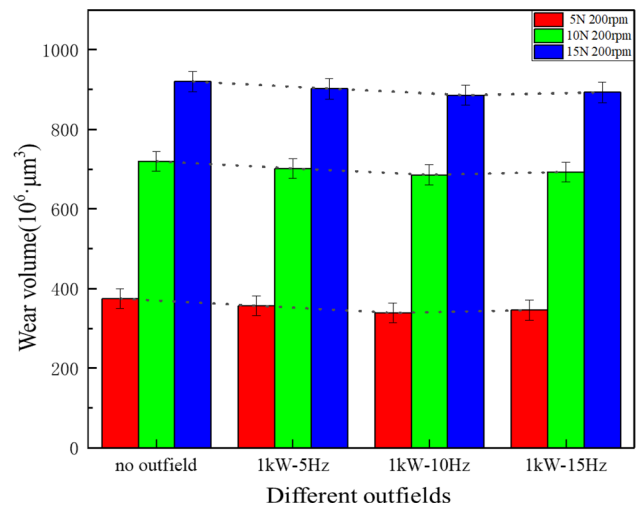
Therefore, in the process of friction and wear, the deformation of the composite material is more uniform, and it is not easy to produce local stress concentration so that the wear surface material is not easy to fall off so that the possibility of adhesive wear is reduced. In addition, the two kinds of reinforced particles and the matrix are pure and closely combined, which reduces the tendency of particles to fall off from the matrix during the friction and wear process, thus reducing abrasive wear.

Results

The Friction and Wear Behavior of (AlB$_2$ + Al$_2$O$_3$)/A356 Composites Controlled by Acoustic-Magnetic Coupling

Effect of Load on Wear Resistance

Figures 8 and 9 are the wear rate and wear volume of 6 wt% (AlB$_2$ + Al$_2$O$_3$)/A356 composites prepared at different magnetic field frequencies under different loads. As the load increases, the wear of all materials increases to a certain extent. Under the same load, the wear volume and wear rate of the composites prepared by the acoustic-magnetic coupling external field control during the preparation process are lower than those of the composites prepared by the non-acoustic-magnetic coupling external field control. This shows that the acoustic-magnetic coupling external field regulation during the reaction process significantly improves the material's wear resistance, and the acoustic-magnetic coupling external field regulation

makes the material grain refinement and enhances the material's wear resistance using fine grain strengthening. Under the same load, when the magnetic field frequency is 10 Hz, the wear rate of 6 wt% (AlB$_2$ + Al$_2$O$_3$)/A356-1 kW-10 Hz composite is 22.9% (5 N), 31.2% (10 N) and 33.5% (15 N) lower than that of 6 wt% (AlB$_2$ + Al$_2$O$_3$)/A356, respectively. From Figure 9, almost all materials decrease as the load increases. There are two reasons for this: the change of wear mechanism, from sticky wear to grinding grain wear, thus reducing the wear strength. On the other hand, during the wear process, the adhesive wear-peeling material is welded to the material surface, and the wear rate is reduced.

Figure 10 shows a scanning electron microscope analysis of the wear morphology of 6 wt% (AlB$_2$ + Al$_2$O$_3$)/A356 composites and 6 wt% (AlB$_2$ + Al$_2$O$_3$)/A356-1 kW-10 Hz composite under different loads. From the analysis of Figure 10a–c, it is found that there are furrows and peeling layers in the wear morphology of 6 wt% (AlB$_2$ + Al$_2$O$_3$)/A356 composites. The flat and precise grooves and fine peeling layer on the wear surface of 6 wt% (AlB$_2$ + Al$_2$O$_3$)/A356 composite indicate that the wear mechanism is mainly abrasive and has slight adhesive wear. From Figure 10d–f, it can be seen that the wear surface of the 6 wt% (AlB$_2$ + Al$_2$O$_3$)/A356-1 kW-10 Hz composite material can hardly see the spalling layer, only some grooves and some debris, and the wear mechanism is mainly slight abrasive wear, which also shows that the addition of the acoustic-magnetic coupling field in the preparation process improves the wear resistance of the material.
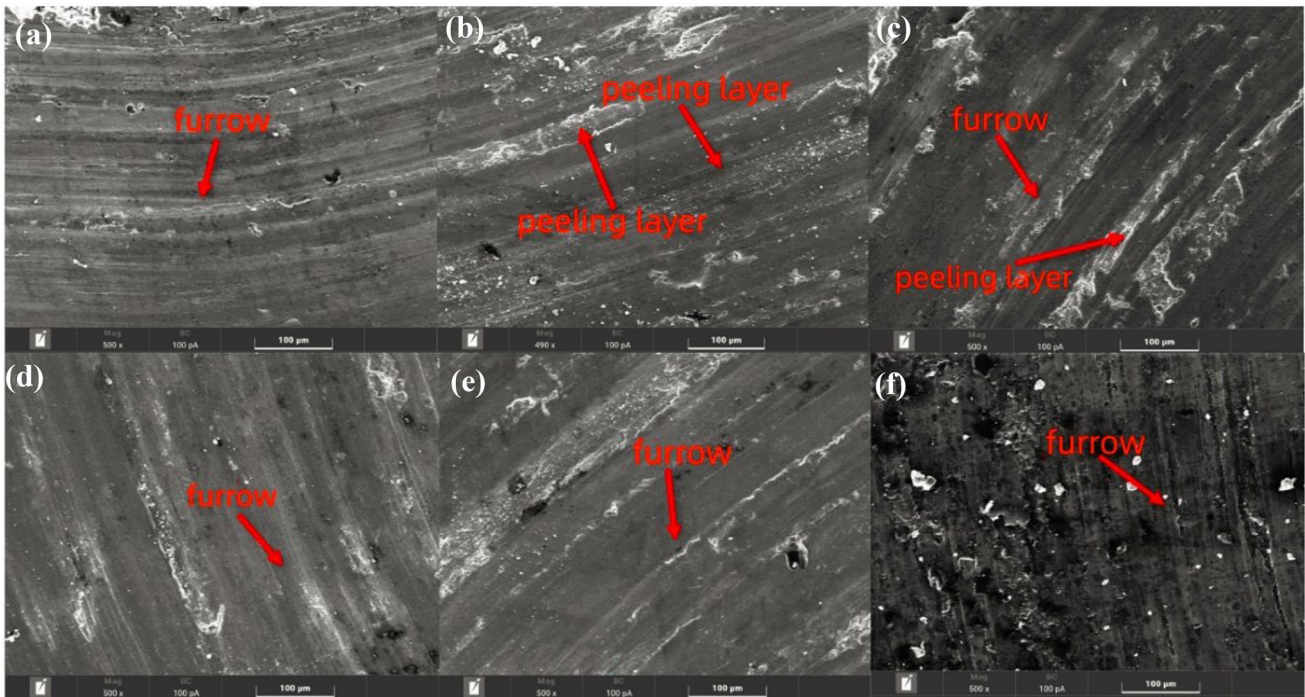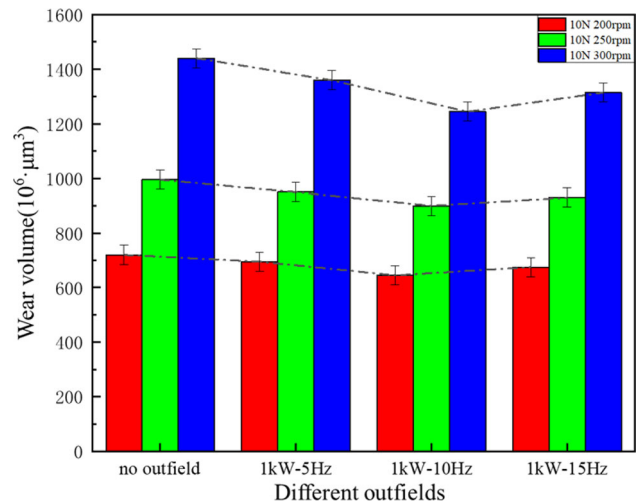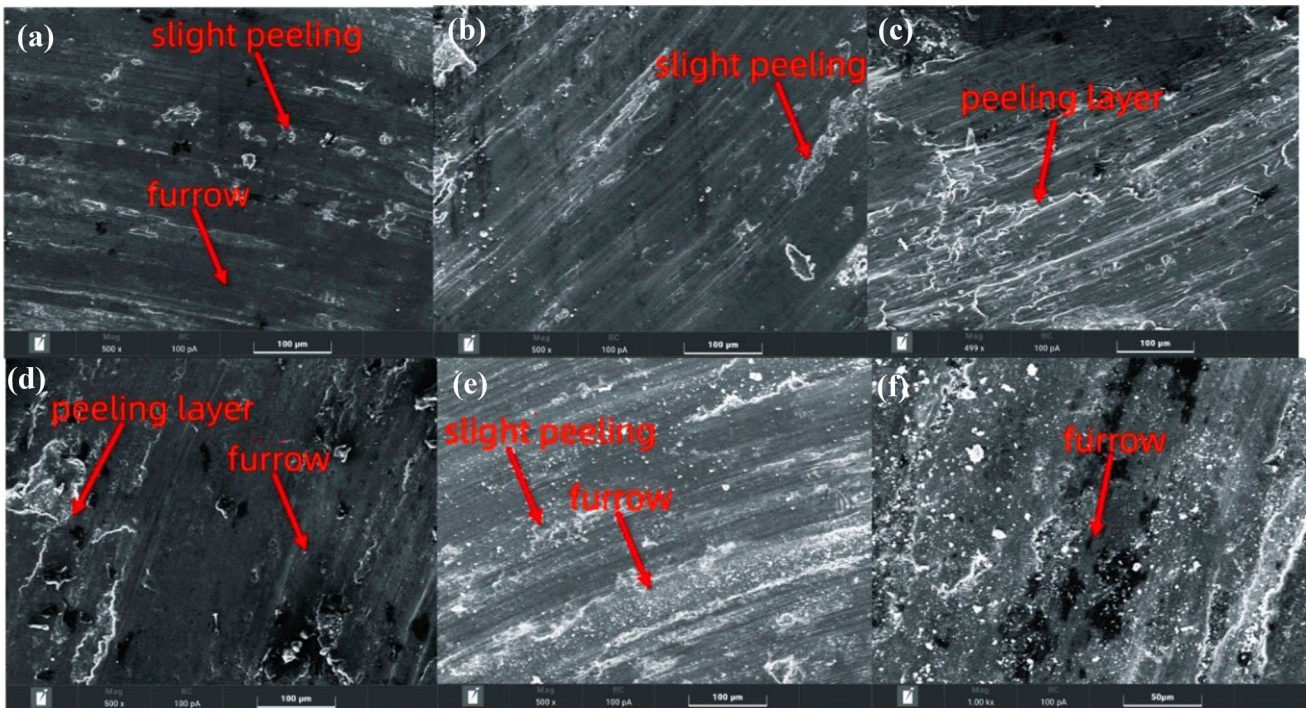
Figure 10. SEM images of wear morphologies of 6 wt% (AlB$_2$ + Al$_2$O$_3$)/A356 composite and 6 wt% (AlB$_2$ + Al$_2$O$_3$)/A356-1 kW-10 Hz composite under different loads (a, b, c) (AlB$_2$ + Al$_2$O$_3$)/A356 composite; (d, e, f) 6 wt% (AlB$_2$ + Al$_2$O$_3$)/A356-1 kW-10 Hz composite; (a, d) 5 N; (b, e) 10 N; (c, f) 15 N.
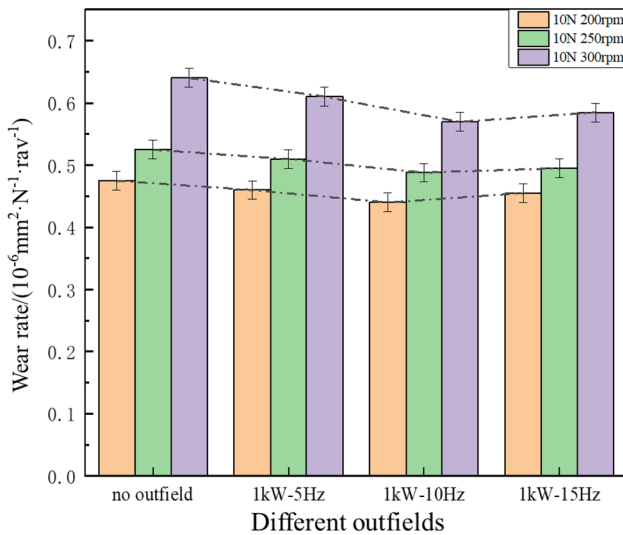
Figure 11. Wear rate of 6 wt% (AlB$_2$+Al$_2$O$_3$)/A356 composites prepared at different magnetic field frequencies composite under different rotating speed.

Figure 12. Wear volume of 6 wt% (AlB$_2$+Al$_2$O$_3$)/A356 composites prepared at different magnetic field frequencies composite under different rotating speed.

Effect of Rotational Speed on Wear Resistance

Figures 11 and 12 are the wear rate and wear volume of 6 wt% (AlB$_2$ + Al$_2$O$_3$)/A356 composites prepared under different magnetic field frequencies at different rotational speeds. The wear volume and wear rate of all materials increase to a certain extent with the increase in rotational speed, and the wear of composites prepared under the regulation of acoustic-magnetic coupling external field is better than that of composites prepared without acoustic-magnetic coupling external field regulation at the same rotational speed. At different speeds, the addition of acoustic-magnetic coupling field control in the reaction is beneficial to improve the material's wear resistance. When the magnetic field frequency reaches 10 Hz, the wear of 6 wt% (AlB$_2$ + Al$_2$O$_3$)/A356-1 kW-10 Hz composites is the most reduced compared with 6 wt% (AlB$_2$ + Al$_2$O$_3$)/A356 composites, reaching 31.2% (200 rpm), 27.2% (250 rpm), and 28.4% (300 rpm), respectively.

Figure 13. *SEM images of wear morphologies of 6 wt% (AlB$_2$ + Al$_2$O$_3$)/A356 composite and 6 wt% (AlB$_2$ + Al$_2$O$_3$)/A356-1 kW-10 Hz composite under different loads (a, b, c) (AlB$_2$ + Al$_2$O$_3$)/A356 composite; (b, c, d) 6 wt% (AlB$_2$ + Al$_2$O$_3$)/A356-1 kW-10 Hz composite; (a, d) 200 rpm; (b, e) 250 rpm; (c, f) 300 rpm.*

Figure 13 shows the wear morphology of 6 wt% (AlB$_2$ + Al$_2$O$_3$)/A356 composites and 6 wt% (AlB$_2$ + Al$_2$O$_3$)/A356-1 kW-10 Hz composite. From Figure 13, the wear of 6 wt% (AlB$_2$ + Al$_2$O$_3$)/A356-1 kW-10 Hz composite is significantly better than that of 6 wt% (AlB$_2$+Al$_2$O$_3$)/A356 composites. When the rotation speed is increased to 300 rpm, the white oxide on the surface of the two materials indicates that the main wear mechanism is oxidative wear. This is due to the large amount of friction heat generated at high speed, which makes the material's surface more easily oxidized. In Figure 13c, f, it can be seen that the wear layer of the 6 wt% (AlB$_2$ + Al$_2$O$_3$)/A356-1 kW-10 Hz composite is significantly less than that of the 6 wt% (AlB$_2$ + Al$_2$O$_3$)/A356 composite. Some oxides and grooves indicate that the wear mechanism of 6 wt% (AlB$_2$ + Al$_2$O$_3$)/A356-1 kW-10 Hz composite is oxidation wear and abrasive wear.

## Analysis of High-Temperature Friction Results

T6 Heat Treatment

The main elements in A356 aluminum alloy are Al, Mg, and Si. The needle-like Si phase forms stress concentrations. The second phase Mg$_2$Si formed also forms segregation during the casting process of the alloy.[42] Therefore, the properties of the alloy can be optimized by heat treatment, and the A356 aluminum alloy and 6 wt% (AlB$_2$ + Al$_2$O$_3$)/A356 composites were treated by T6.

Figure 14 is the peak aging diagram of A356 alloy and 6 wt% (AlB$_2$ + Al$_2$O$_3$)/A356-1 kW-10 Hz composite after T6 treatment, and it is evident that the T6 treatment has led to an enhancement in the hardness of the cast aluminum alloy A356. The aging peak hardness of 6 wt% (AlB$_2$ + Al$_2$O$_3$)/A356-1 kW-10 Hz composite is about twice that of A356 alloy. This is because the hardness of AlB$_2$ and Al$_2$O$_3$ nanoparticles is much higher than that of aluminum matrix, which can give its intrinsic hardness to the matrix. Adding a stronger and harder reinforcing phase to the aluminum matrix can effectively hinder the movement of dislocations, thereby improving the hardness and strength of the nanocomposites.

Figure 15a shows the scanning image of A356 alloy after T6 treatment. Mg$_2$Si is continuously precipitated at the grain boundary and connected into a network structure. At this time, the number of Mg$_2$Si is more. Figure 15b is the scanning image of 6 wt% (AlB$_2$ + Al$_2$O$_3$)/A356-1 kW-10 Hz composites after T6 treatment. The network structure of Mg$_2$Si is broken and spheroidized, and a large amount of Mg$_2$Si is dissolved into the matrix. The peak time of the material increases after the addition of reinforcing particles since AlB$_2$ and Al$_2$O$_3$ at the matrix α-Al grain boundary hinder the precipitation of Mg$_2$Si during the artificial aging process and prolong the artificial aging time.
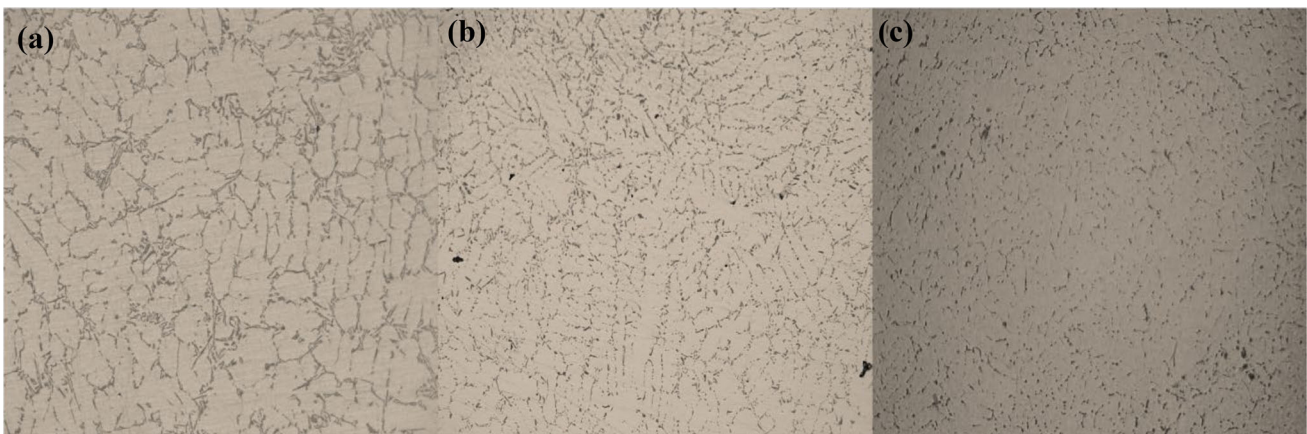
From Figure 16, Si in A356 alloy mainly exists as disordered needles. T6 treatment can first dissolve the second
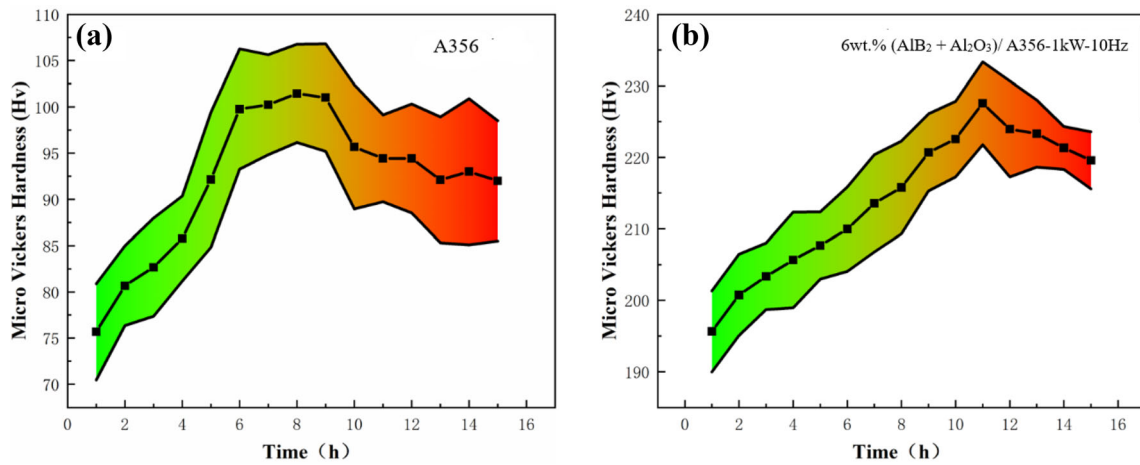
Figure 14. *Aging peak graph for A356 and 6 wt% (AlB₂ + Al₂O₃)/A356-1 kW-10 Hz (a) A356 (b) 6wt% (AlB₂ + Al₂O₃)/A356-1 kW-10 Hz.*
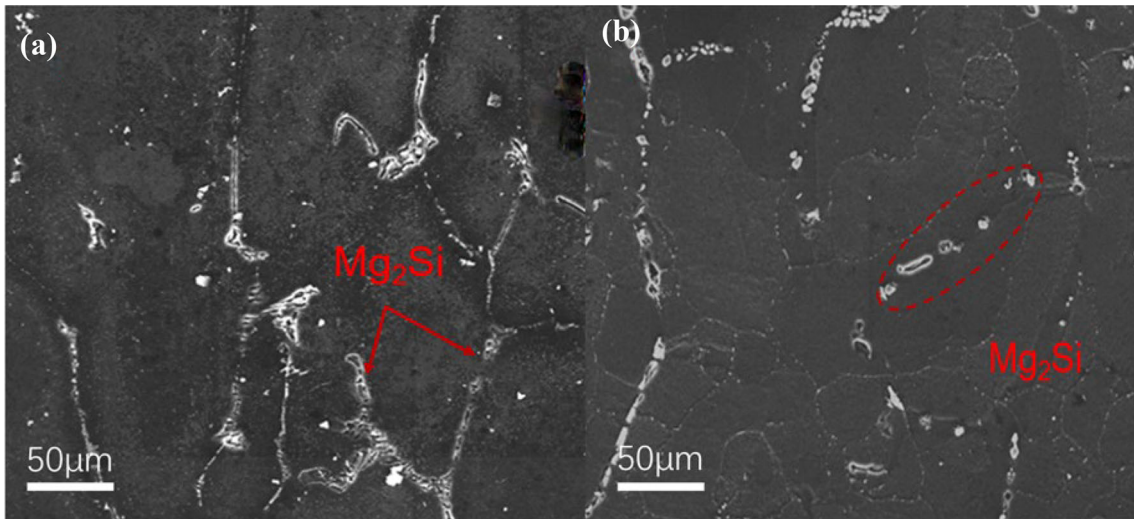
Figure 15. *SEM of A356-T6 and 6 wt% (AlB₂ + Al₂O₃)/A356-1 kW-10 Hz-T6.*

Figure 16. *Metallographic images of A356 alloy, A356-T6 alloy and 6 wt% (AlB₂ + Al₂O₃)/A356-1 kW-10 Hz-T6 composite (a) A356 (b) A356-T6 (c) 6 wt% (AlB₂ + Al₂O₃)/A356-1 kW-10 Hz-T6.*

phase and solute atoms into the alloy through the solid solution process for homogenization treatment and spheroidization of Si, followed by the precipitation of the second phase in the supersaturated state through the aging process. The precipitated second phase can effectively pin the dislocation to improve the alloy performance. After the T6 treatment, the needle-like material in the metallographic diagram of A356 alloy is reduced, and the distribution is more uniform. The needle-like Si can hardly be seen in the metallographic diagram of the T6-treated composite because the addition of the two-phase particles has a limiting effect on the growth of Si.
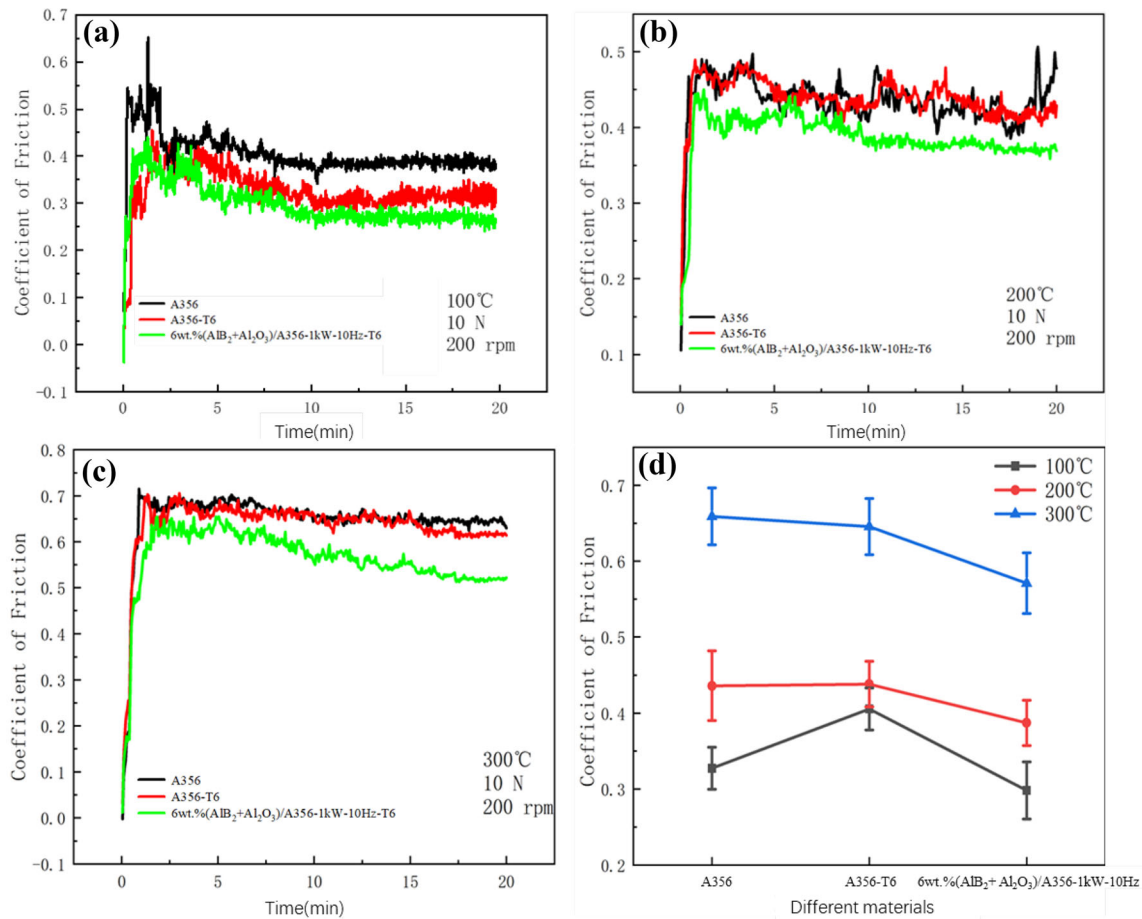
Effect of Temperature on Friction Coefficient

Figure 17 illustrates the variation curves of friction coefficient with temperature for A356 alloy, A356-T6 alloy, and 6 wt% (AlB$_2$ + Al$_2$O$_3$)/A356-1 kW-10 Hz-T6. The increased hardness of the T6 treatment increases the frictional strength and coefficient of friction of the material surface to some extent compared to the A356 and A356-T6 alloy. The friction coefficient of 6 wt% (AlB$_2$ + Al$_2$O$_3$)/A356-1 kW-10 Hz composites with dual-phase particles

after T6 treatment is still lower than that of A356 and A356-T6. The results reveal that the anti-friction effect of the dual-phase particles on the material remains effective at high temperatures.

As the friction temperature increases, the friction coefficient of all materials increases to varying degrees. It is related to the softening of the material surface caused by the increase in temperature, which makes more friction surfaces peel off during the friction process, increasing the roughness of the surface. At various temperatures, the friction coefficients of 6 wt% (AlB$_2$ + Al$_2$O$_3$)/A356-1 kW-10 Hz composites decrease by 10.9% and 26.5% at 100 °C, 11.2% and 13.7% at 200 °C, and 13.4% and 11.5% at 300 °C.
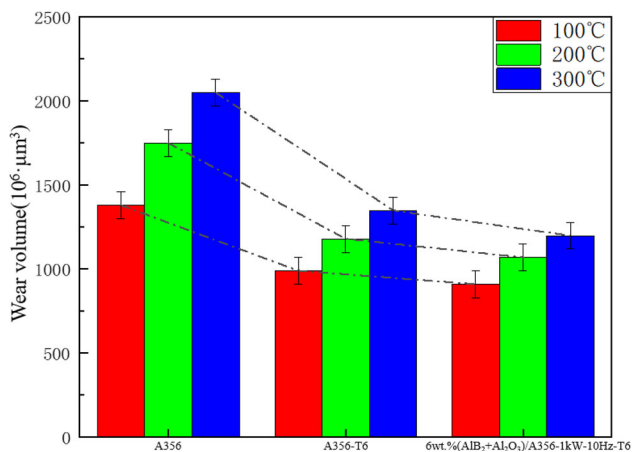
Effect of Temperature on Wear Resistance

Figures 18 and 19 are the wear rate and volume of A356 alloy, A356-T6 alloy, and 6 wt% (AlB$_2$ + Al$_2$O$_3$)/A356-1 kW-10 Hz-T6 composite at different temperatures. Comparing A356 alloy with A356-T6 alloy, the T6 treatment enhances the material's wear resistance. The wear

Figure 17. Coefficient of friction of different materials at (a) 100 °C; (b) 200 °C; (c) 300 °C; (d) average friction coefficient.
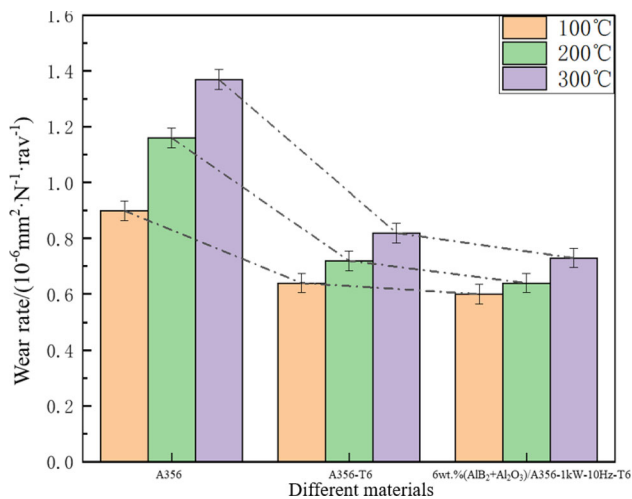
Figure 18. Wear rate of A356 alloy, A356-T6 alloy and 6 wt% (AlB₂ + Al₂O₃)/A356-1 kW-10 Hz-T6 composite at different temperatures.

Figure 19. Wear volume of A356 alloy, A356-T6 alloy and 6 wt% (AlB₂ + Al₂O₃)/A356-1 kW-10 Hz-T6 composite at different temperatures.

rate and volume of the 6 wt% $(AlB_2 + Al_2O_3)$/A356-1 kW-10 Hz-T6 composite is lower than those of the A356-T6 alloy for the same friction temperature, further indicating that the addition of duplex-phase particles has a significant effect on the wear resistance of the material on the one hand. On the other hand, the wear resistance of the composite at high temperatures is still better than that of the matrix alloy, which indicates that the material's wear resistance is still significantly improved by the dual-phase particles at high temperatures. At different temperatures, respectively, the wear rates of 6 wt% $(AlB_2 + Al_2O_3)$/A356-1 kW-10 Hz-T6 composites were reduced by 33.1% and 8.8% (100 °C), 42.6% and 11.3% (200 °C), 46.4% and 13.7% (300 °C), compared with A356 alloy and A356-T6 alloy.

Figure 20 shows the SEM analysis of the wear morphology of A356 alloy, A356-T6 alloy, and 6 wt% $(AlB_2 + Al_2O_3)$/
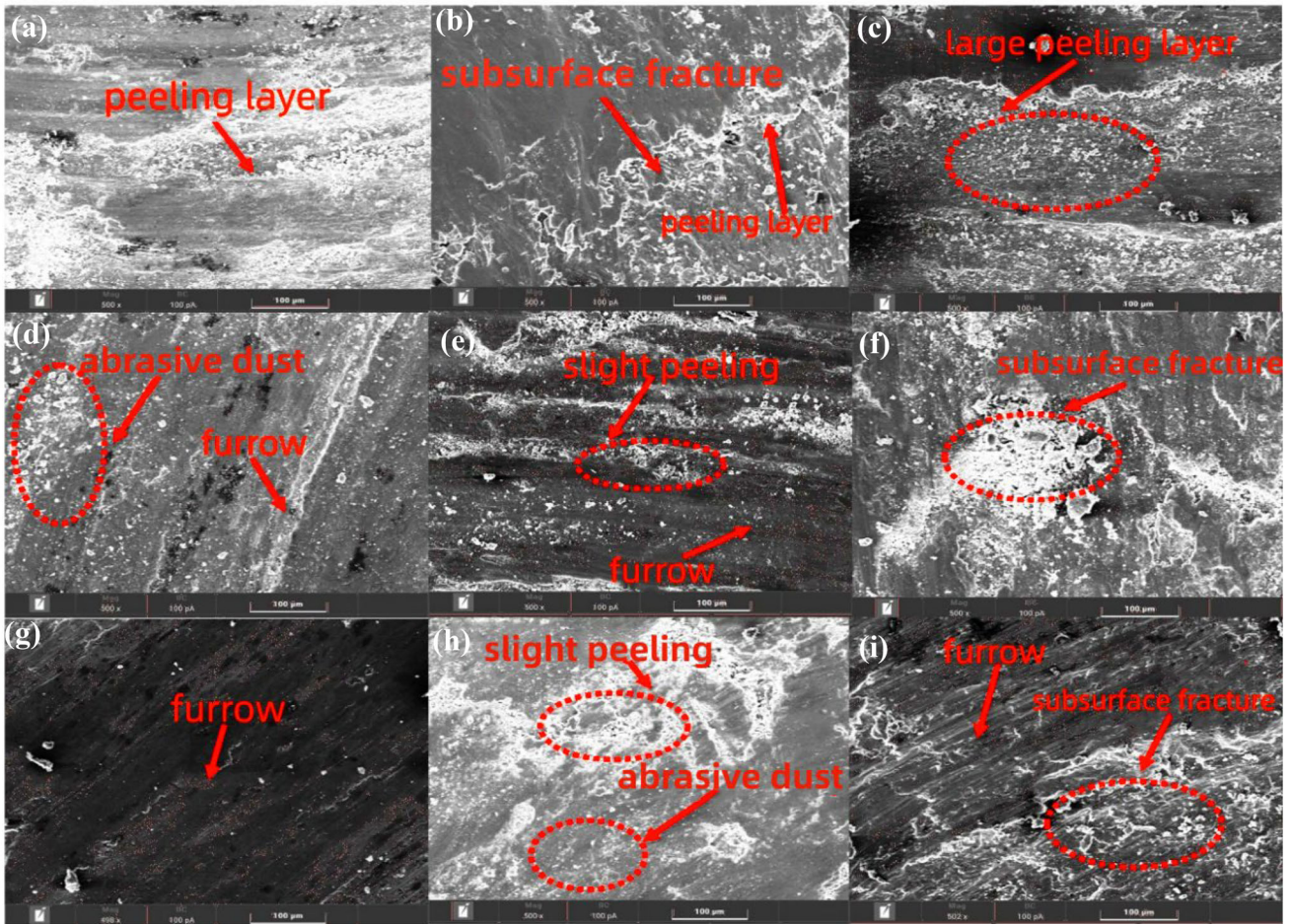
A356-1 kW-10 Hz-T6 composite at different temperatures. When the friction temperature is 100 °C, the friction surface (a, b, c) of A356 alloy has different degrees of spalling layer and sub-surface fracture. This is attributed to the fact that the surface of the A356 alloy is softened at high temperatures and the main wear mechanism is adhesive wear. Combined with Figures (d, e, f) and Figures (g, h, i), the surface wear of A356-T6 alloy and 6 wt% $(AlB_2 + Al_2O_3)$/A356-1 kW-10 Hz-T6 composite is similar, and the wear of the composite is slightly better. The addition of dual-phase particles reduces the friction coefficient on the material surface and decreases the friction strength between the friction pairs. Both materials dominate by abrasive wear at a friction temperature of 100 °C. When the temperature rises to 300 °C, sub-surface fracture occurs, and the wear mechanism is mainly adhesive wear. The surface of the materials has large deformation, such as pits and sub-surface fractures. Moreover, the heat generated during the friction process causes the oxidation of the friction surface, and the color of different regions is different. A prominent peeling layer was found on the wear surface. This is because the high temperature softens the material on the friction surface and is not enough to firmly bond with the material below, thus causing the surface to fall off. These are the characteristics of adhesive wear.

Figures 21, 22, and 23 are the 3D confocal images of the wear morphology of A356 alloy, A356-T6 alloy, and 6 wt% $(AlB_2 + Al_2O_3)$/A356-1 kW-10 Hz-T6 composites at 100 °C, 200 °C and 300 °C. At the friction temperature of 100 °C, the wear scar of the composite is reduced by 17.1% and 5.5% compared with A356 alloy and A356-T6 alloy; at 200 °C, the wear scar of the composite is reduced by 31.5% and 16.6% compared with A356 alloy and A356-T6 alloy; and at 300 °C, the wear scar of the composites decreases by 40.4% and 19.2%, respectively, compared with that of A356 alloy and A356-T6 alloy. The wear scar depth of the composites is much lower than that of A356 alloy and A356-T6, which further shows that the wear resistance of the composites is still significantly improved compared with the matrix alloy in a high-temperature environment.

Discussion

Synergy Action of Ultrasonic Field and Magnetic Field

Figure 24 shows a schematic diagram of the forced convection of the melt caused by the coupling field. The two physical fields stir the melt from different directions. The ultrasonic flow motion generated by the ultrasonic field occurs along the axis of the horn, and the action caused by the magnetic field is tangential to the horn. The intense vibration effect of the coupling field helps to prevent the formation of clusters and disperse the existing clusters in

Figure 20. SEM images of wear morphologies of A356 alloy, A356-T6 alloy, and 6 wt% (AlB$_2$ + Al$_2$O$_3$)/A356-1 kW-10 Hz-T6 composite at different temperatures (a, d, g) 100 °C; (b, e, h) 200 °C; (c, f, i) 300 °C; (a, b, c) A356 alloy; (d, e, f) A356-T6 alloy; (g, h, i) 6 wt% (AlB$_2$ + Al$_2$O$_3$)/A356-1 kW-10 Hz-T6 composite.
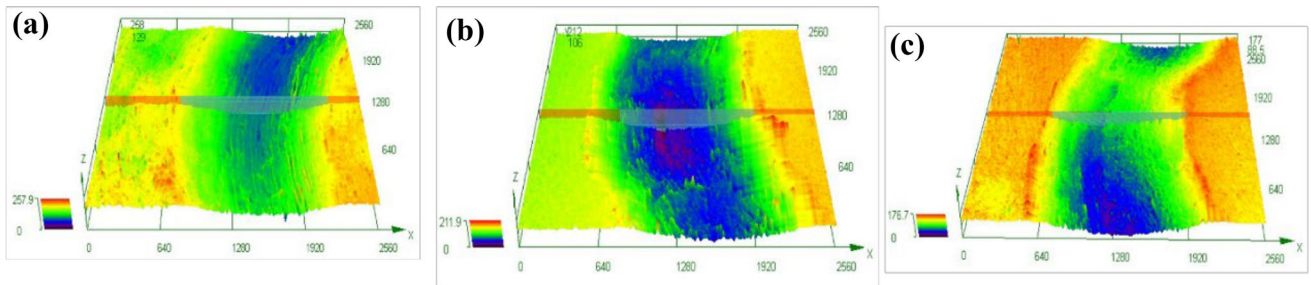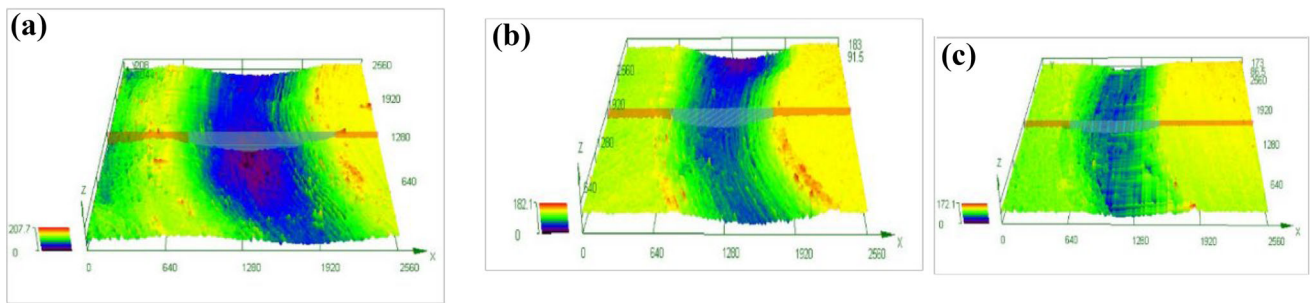

Figure 21. Three-dimensional confocal images of wear morphologies of A356 alloy, A356-T6 alloy and 6 wt% (AlB$_2$ + Al$_2$O$_3$)/A356-1 kW-10 Hz-T6 composite at 100 °C.

the melt, thereby refining the particles. In addition, contact friction occurs between particles under an external physical field, making the particles more rounded and producing a spheroidizing effect. Meanwhile, the particle clusters are broken, resulting in particle refinement. The coupling field helps complete the reaction and heat transfer of the entire melt, ensuring a uniform concentration in each melt region to inhibit particle growth. In summary, coupled fields can homogenize nanoparticle distribution, reduce the size and improve nanoparticle morphology. Therefore, the coupling

of ultrasonic and magnetic fields not only solves the problems associated with individual physical fields, but also amplifies the advantages of these fields.

When coupled magnetic and ultrasonic magnetic fields are applied to the melt, the magnetic and ultrasonic fields act differently. The magnetic force and joule heat generated by the magnetic field increase the nanoparticle volume fraction and facilitate the reaction process. Firstly, the magnetization of the reactants and molten aluminum generates

Figure 22. Three-dimensional confocal images of wear morphologies of A356 alloy, A356-T6 alloy and 6 wt% (AlB₂ + Al₂O₃)/A356-1 kW-10 Hz-T6 composite at 200 °C.
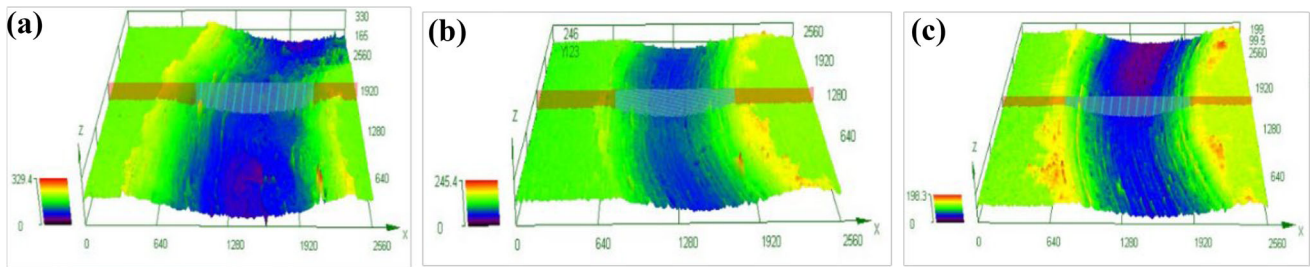
Figure 23. Three-dimensional confocal images of wear morphologies of A356 alloy, A356-T6 alloy and 6 wt% (AlB₂ + Al₂O₃)/A356-1 kW-10 Hz-T6 composite at different 300 °C.
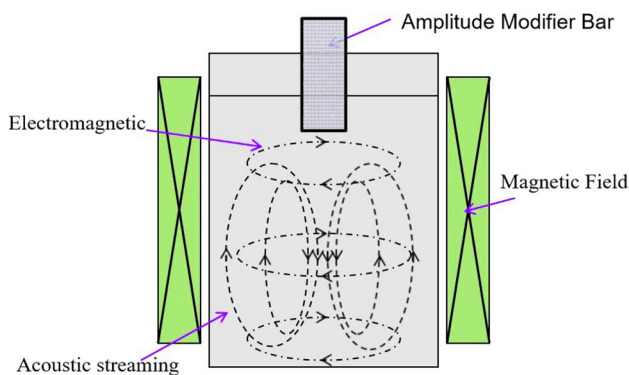
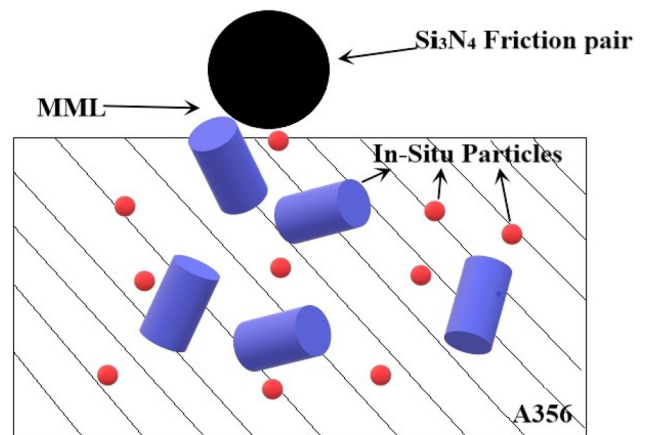*Figure 24. Schematic diagram of the forced convection in the melt under the acoustic-magnetic coupling field.*

Figure 25. Tribological behavior model diagram of composites.

eddy currents on the surface, leading to the involvement of more reactants in the reaction, increasing the reaction products (Al_2O_3 and AlB_2). Secondly, adding a rotating electromagnetic field can cause the rotation of the melt, aggravate the energy and structural fluctuation, and promote the nucleation to refine the grain.[43] It can also accelerate the mixing of the aluminum matrix and reinforcing particles, thus improving the distribution of nanoparticles in the composites.

Analysis of Frictional Behavior

The friction and wear model of the composites is shown in Figure 25. Due to the mechanical alloying mechanism, a mechanically mixed layer (MML) is formed on the wear surface. When a thin layer of MML with high hardness is formed, the frictional properties of the material can be improved. The MML formed by AlB_2 particles and Al_2O_3 particles can achieve the above effect. When there are AlB_2 and Al_2O_3 particles in the friction material, the MML with micro-protrusions can reduce the friction contact surface and even play a particular lubrication role, thus reducing and stabilizing the friction coefficient. In addition, Al_2O_3 particles and AlB_2 particles can play the role of Orowan strengthening and refining the structure. The refined structure increases the grain boundary area of the material and the resistance to dislocation movement. The grain refinement leads to an increase in the number of grains, and the movable slip system also increases so that the

deformation during the wear process can be evenly distributed to more grains, thereby improving the material's wear resistance (Figure 25).

Conclusion

(1) The microstructure of $(AlB_2 + Al_2O_3)$/A356 composites were analyzed. The dual-phase particles have a refining effect on the matrix α-Al grains. The grain size of the A356 matrix alloy decreases with increasing particle mass fraction. When the particle mass fraction is 6 wt%, the A356 matrix grain size is the smallest, and no large particle agglomeration is found. Polarized light microscopy, SEM and EDS characterization of 6 wt% $(AlB_2 + Al_2O_3)$/A356 composites with applied acoustic-magnetic coupling field revealed that the acoustic-magnetic coupling field control could effectively reduce the particle size. The AlB_2 particles are micron-sized rod-shaped, and the Al_2O_3 particles are nano-sized. When the magnetic field frequency is 10 Hz, and the ultrasonic power is 1 kW, the matrix α-Al grain refinement effect is the best.

(2) After T6 treatment of A356 alloy and 6 wt% $(AlB_2 + Al_2O_3)$/A356-1 kW-10 Hz composite, it is found that the peak aging time of 6 wt% $(AlB_2 + Al_2O_3)$/A356-1 kW-10 Hz composite is larger than that of A356 alloy. After adding the reinforced particles, the peak time of the material also increases. The AlB_2 and Al_2O_3 at the grain boundary of the matrix α-Al hinder the precipitation of Mg_2Si during the artificial aging process and prolong the artificial aging time.

(3) Compared with A356 alloy and A356-T6 alloy, the 6 wt% $(AlB_2 + Al_2O_3)$/A356-1 kW-10 Hz-T6 composite has the best wear resistance and the smallest friction coefficient, and the composite has the shallowest wear scar depth. The wear rate of 6 wt% $(AlB_2 + Al_2O_3)$/A356-1 kW-10 Hz-T6 composite is reduced by 33.08% and 8.82% (100 °C), 42.55% and 11.29% (200 °C), 46.44% and 13.69% (300 °C), respectively, compared with A356 alloy and A356-T6 alloy. $(AlB_2 + Al_2O_3)$ dual-phase particles significantly improve the frictional wear properties of the material, even at high temperatures. The introduction of particles makes the primary wear mechanism of each material different. The A356 alloy is subject to adhesive wear, while the A356-T6 and 6 wt% $(AlB_2 + Al_2O_3)$/A356-1 kW-10 Hz-T6 composites are subject to abrasive wear.

REFERENCES

1. G.H.S. Gava, R.M.D. Souza, J.D.B. de Mello, M.C.S. de Macêdo, C. Scandian, Effect of load partition and particle distribution on micro-abrasive wear mapping of two-phase metal matrix composites. Wear **301**(1), 130–136 (2013)
2. W. Wolf, E.M. Mazzer, The influence of particle size and heat treatments on the transformation energies of a gas atomized Cu-Al-Ni-Mn shape memory alloy. Thermochim. Acta **707**, 158–168 (2022)
3. H. Mao, C. Li, Y. Dong et al., The effect of Mn on particles morphology and property of 5 wt% TiB_2/Al-4.5Cu-0.4Mn alloys. J. Alloys Compd. **904**, 23–31 (2022)
4. K. Su, Q. Zhang, H. Hou et al., Properties and microstructure evolution of unfired Al–Si incorporated Al_2O_3–C slide plate materials with trace nano-Al_2O_3 particles. Ceram. Int. **47**(23), 33641–33650 (2021)
5. P. Zhang, X. Yue, Q. Zhang et al., Investigation on the influence of SiC particle parameters on the machinability of SiCp/Al composite. Vacuum **191**, 56–67 (2021)
6. M. Balakrishnan, I. Dinaharanc, R. Palanivel et al., Influence of friction stir processing on microstructure and tensile behavior of AA6061/Al3Zr cast aluminum matrix composites. J. Manuf. Process. **38**, 148–157 (2019)
7. R. Vasanth Kumara, R. Keshavamurthyb, C.S. Peruguc et al., Influence of hot rolling on microstructure and mechanical behaviour of Al6061-ZrB_2 in-situ metal matrix composites. Mater. Sci. Eng. A **738**, 344–352 (2018)
8. B. Kumar, P. Kumar, Preparation of hybrid reinforced aluminium metal matrix composite by using ZrB_2: a systematic review. Mater. Today Proc. **61**, 115–120 (2022)
9. Y. Liu, R. Wang, C. Peng et al., Microstructures and mechanical properties of in-situ TiB_2/Al–xSi–0.3Mg composites. Nonferrous Met. Soc. China **31**, 331–344 (2021)

10. M. Mallik, P. Mitra, N. Srivastava et al., Abrasive wear performance of zirconium diboride based ceramic composite. Int. J. Refract. Met. Hard Mater. **79**, 224–232 (2019)

11. X.C. Tong, A.K. Ghosh, Fabrication of in situ TiC reinforced aluminum matrix composites. J. Mater. Sci. **36**, 4059–4069 (2001)

12. Z. Fan, Y. Wang, Y. Zhang et al., Grain refining mechanism in the Al/Al–Ti–B system. Acta Mater. **84**, 292–304 (2015)

13. C.-Y. Liu, G.-B. Teng, Z.-Y. Ma et al., Effects of Sc and Zr microalloying on the microstructure and mechanical properties of high Cu content 7xxx Al alloy. Int. J. Miner. Metall. Mater. **26**(12), 1559–1569 (2019)

14. Q. Yan, G. Chen, Z. Zhang et al., In-situ fabrication of submicron α-Al_2O_3 particle reinforced $AlSi_9Cu_3$ alloy matrix composites by TIG arc process. Mater. Res. Express **6**(6), 489–497 (2019)

15. H. Su, W. Gao, Z. Feng et al., Processing, microstructure and tensile properties of nano-sized Al_2O_3 particle reinforced aluminum matrix composites. Mater. Des. **1980–2015**(36), 590–596 (2012)

16. M. Karbalaei Akbari, O. Mirzaee, H.R. Baharvandi, Fabrication and study on mechanical properties and fracture behavior of nanometric Al_2O_3 particle-reinforced A356 composites focusing on the parameters of vortex method. Mater. Des. **46**, 199–205 (2013)

17. K. Ajay Kumar, C. Mallikarjuna, Microstructure and mechanical properties of A356/Al2O3/MoS_2 hybrid nanocomposites. Mater. Today Proc. **45**, 77–89 (2021)

18. W. Li, H. Chen, Z. Liang et al., Effects of SiC orientations and particle sizes on the low cycle fatigue properties of SiCp/A356 composite. Int. J. Fatigue **152**, 56–67 (2021)

19. N. Liu, B. Jiang, Y. Wang et al., Influence of trace amount chromium on microstructure and corrosion behavior of A356–5 vol.%TiB_2 alloy. Mater. Lett. **314**, 158–169 (2022)

20. V.M. Zeeshan Ali, P. Rathnakumar, P. Gurusamy, M. Nagaral, Studies on mechanical properties of 3 wt% of 40 and 90 um size B_4C particulates reinforced A356 alloy composites. Mater. Today Proc. **50**, 2214–7853 (2021)

21. J. Zhao, J. Shangguan, C. Gu et al., Effect of electro-spark deposited ZA12 interlayer on the microstructure and mechanical property of A356/AZ91D by liquid-solid compound casting. Mater. Chem. Phys. **278**, 2256–2267 (2022)

22. E. Natesan, S. Eriksson, J. Ahlstrom et al., Effect of temperature on deformation and fatigue behaviour of A356–T7 cast aluminium alloys used in high specific power IC engine cylinder heads. Materials (Basel) **13**(5), 45–61 (2020)

23. Y. Bai, Y. Guo, J. Li et al., Effect of Al_2O_3 nanoparticle reinforcement on the mechanical and high-temperature tribological behavior of Al-7075 alloy. Proc. Inst. Mech. Eng. Part J J. Eng. Tribol. **231**(7), 900–909 (2016)

24. K. Yang, L. An, L. Cheng, Microstructure and tribological behavior of Al_2O_3 particle reinforced Al matrix composites fabricated by spark plasma sintering. J. Wuhan Univ. Technol.-Mater. Sci. Ed. **34**(5), 1013–1017 (2019)

25. S. Agrawal, A.K. Ghose, I. Chakrabarty, Effect of rotary electromagnetic stirring during solidification of In-situ Al-TiB_2 composites. Mater. Des. **113**, 195–206 (2017)

26. L. Yuan, J. Han, J. Liu et al., Mechanical properties and tribological behavior of aluminum matrix composites reinforced with in-situ AlB_2 particles. Tribol. Int. **98**, 41–47 (2016)

27. X. Liu, X. Shi, Y. Huang et al., Anti-friction and wear properties of the friction surface of M50–10 wt%(50Sn40Ag10Cu) composite. J. Alloys Compd. **765**, 7–17 (2018)

28. M. Bin, Z.M. Jian, Study of anti-friction performance of spherical FeS nanoparticle. Appl. Mech. Mater. **475–476**, 1334–1339 (2013)

29. G. Chen, X. Song, N. Hu et al., Effect of initial Ti powders size on the microstructures and mechanical properties of Al_3Ti/2024 Al composites prepared by ultrasonic assisted in-situ casting. J. Alloys Compd. **694**, 539–548 (2017)

30. L.Z.Y. Jiao, Preparation and wear properties of (Al_3Zr+ZrB_2)P/2124 composites material with in-situ proces. Adv. Mater. Res. **600**, 199–203 (2012)

31. L. Qi, Z. Li, Q. Zhang et al., Electromagnetic stirring control for resistance spot welding of SiCp/Al composites. J. Manuf. Process. **68**, 1271–1279 (2021)

32. M. Li, N. Omura, Y. Murakami et al., A comparative study of the primary phase formation in Al–7 wt% Si and Al–17 wt% Si alloys solidified by electromagnetic stirring processing. Mater. Today Commun. **24**, 667–679 (2020)

33. Y. Zhang, R. Li, P. Chen et al., Tuning the microstructure morphology and genetic mechanical properties of 2219 Al alloy with ultrasonic treatment. J. Alloy. Compd. **846**, 675–685 (2020)

34. Y. Jia, D. Song, N. Zhou et al., The growth restriction effect of TiCN nanoparticles on Al-Cu-Zr alloys via ultrasonic treatment. Ultrason. Sonochem. **80**, 105829 (2021)

35. Z. Liu, T. Zhu, Y. Jia et al., Preparation of in-situ TiB_2 reinforced aluminum matrix composites assisted by two steps of ultrasonic vibration. Mater. Res. Express **8**(4), 046506 (2021)

36. S. Ramani, K.L.D. Wins, J. Nampoothiri et al., Effect of post-reaction ultrasonic treatment on synthesis, microstructural evolution, and mechanical behavior of Al4043/TiB_2 in situ nanocomposites. Arab. J. Sci. Eng. **46**, 7521–7531 (2021)

37. J. Lei, Wu. Zhao Yutao, Yue, et al., Microstructures of in-situ TiB_2/7055Al composites by the ultrasonic and

magnetic coupled field. Surf. Topogr. Metrol. Prop. **9**(1), 015026 (2021)

38. R. Tao, Y. Zhao, X. Kai et al., Microstructures and properties of in situ ZrB_2 /AA6111 composites synthesized under a coupled magnetic and ultrasonic field. J. Alloy. Compd. **754**, 114–123 (2018)

39. R. Tao, Y. Zhao, X. Kai et al., Effects of hot rolling deformation on the microstructure and tensile properties of an in situ-generated ZrB_2 nanoparticle-reinforced AA6111 composite. Mater. Sci. Eng. A **732**, 138–147 (2018)

40. S. Zhang, Y. Zhao, G. Chen et al., $(Al_2O_3 + Al_3Zr)$/A356 nanocomposites fabricated by magnetochemistry in situ reaction. J. Alloys Compd. **475**, 261–267 (2009)

41. X. Kai, S. Huang, L. Wu et al., High strength and high creep resistant ZrB_2/Al nanocomposites fabricated by ultrasonic-chemical in-situ reaction. J. Mater. Sci. Technol. **35**, 2107–2114 (2019)

42. F. Meng, H. Huang, X. Yuan et al., Segregation in squeeze casting 6061 aluminum alloy wheel spokes and its formation mechanism. China Foundry **18**, 45–51 (2021)

43. C. Lou, Q. Wang, C. Wang et al., Migration and rotation of $TiAl_3$ particles in an Al-melt solidified under high magnetic field conditions. J. Alloy. Compd. **472**(1–2), 225–229 (2009)